Journal of Catalysis 352 (2017) 466–479

Contents lists available at ScienceDirect

Journal of Catalysis

journal homepage: www.elsevier.com/locate/jcat

Polymer nanofilm-coated catalysis: An approach for enhancing water-resistance of Co-Fe oxide nano-catalysts under moisture-rich condition

Yali Shen [a], Jun Yu [a], Xiuzhen Xiao [a], Xiaoming Guo [a], Dongsen Mao [a], Houjin Huang [a,*], Guanzhong Lu [a,b,*]

[a] Research Institute of Applied Catalysis, School of Chemical and Environmental Engineering, Shanghai Institute of Technology, Shanghai 201418, China
[b] Key Laboratory for Advanced Materials and Research Institute of Industrial Catalysis, East China University of Science and Technology, Shanghai 200237, China

ARTICLE INFO

Article history:
Received 25 January 2017
Revised 31 May 2017
Accepted 16 June 2017

Keywords:
Fe-Co mixed oxide catalyst
Polymer-coated nanoparticles
Water-resistance
CO oxidation
Preparation of nanocatalyst
Modified solid-phase method

ABSTRACT

Water-induced deactivation of the oxides catalysts (especially for the Co_3O_4-based catalysts) is a challenging problem. For this reason, highly effective, long-term stable, moisture-resistant polymer nanofilm-coated $Fe_aCo_bO_x$ catalysts were synthesized by a solid-phase method mediated with oxalic acid (OA)/ethlyene glycol (EG) for low-temperature CO oxidation. The effects of the Fe, OA and EG amounts and calcination temperature on the physicochemical and catalytic properties of the $Fe_aCo_bO_x$ catalysts were investigated by various characterization techniques. The results demonstrate that the $Fe_aCo_bO_x$ catalysts are structurally mesoporous, and nanostructured $Fe_aCo_bO_x$ and polymer nanofilm coating play major roles on their high catalytic activity and stability. The nanofilm-coated $Fe_3Co_{16}O_x$ nanoparticles prepared under an optimized synthetic condition and calcined at 250 °C possesses higher surface area (134 m^2/g), Co^{3+}/Co^{2+} ratio (1.89) and oxygen vacancy (20.5%), and thus exhibits the excellent catalytic performance for CO oxidation, such as, T_{50} of −114 °C under normal moisture (3–10 ppm) and T_{50} of 47 °C under moisture-rich (~0.6 vol.%) conditions. Remarkably, compared with the published results, its much-improved long-term catalytic stability (>1 month) can be observed even at a very high moisture level (3.1 vol.%) and relatively low temperature (90 °C). The deactivation of the catalyst at lower temperature resulted from accumulated water and carbonates on the catalyst surface can also be substantially minimized, through the water vapor-resistant with the help of gas-permeable polymer nanofilm coating.

1. Introduction

CO is a colorless, odorless and very toxic gas for humans and animals. Many kinds of catalysts for the CO oxidation have been reported, including noble metal catalysts and transition metal oxide catalysts [1–6]. For the noble metal catalysts, such as Pt [4,5,7–9], Pd [4,10–12], Au [6,13,14], due to the high cost and scarcity of resources, their commercial applications are limited. On the other hand, with remarkable progresses in transition metal oxide syntheses, the CO oxidation over transition metal oxide catalysts has recently attracted much attention. The transition metal oxide catalysts, such as cobalt oxides [15,16] and copper oxides [17,18], which are low cost and good performance, have been widely studied. Among these, cobalt oxide has been considered as possible substitutes of noble metals because of its high activity for CO oxidation at low temperature [19]. Xie et al. [15] reported that Co_3O_4 nanorods, which predominantly exposed the {1 1 0} plane with richness of active Co^{3+} sites, exhibited high activity and stability for CO oxidation with T_{100} (the reaction temperature of 100% conversion) of −77 °C in a moist stream of normal feed gas. Li et al. [20] reported that adding Fe into Co_3O_4 can increase significantly its catalytic activity, and the $Fe_2Co_8O_x$ can catalyze the complete oxidation of CO to CO_2 at −80 °C. Zhou et al. [21] found that Cu^{2+} substitution for Co^{2+} has almost no influence on the CO adsorption, but it's easy to form oxygen vacancies to enhance the oxygen reactivity of the oxide catalysts, resulting in increasing the catalytic activity of metal oxide catalyst. Jansson et al. [16] thought that octahedrally coordinated surface Co^{3+} was the active sites for CO adsorption, and the active Co^{3+} transformed to Co^{2+} would result in its deactivation. Gu et al. [22] suggested that not only the octahedrally coordinated Co^{3+} is highly active, but also the octahedrally coordinated Co^{2+} species in an inverse spinel structure $CoFe_2O_4$ show some activity, because of the Co^{2+} species can be easily oxidized to Co^{3+}. The cobalt ferrite ($CoFe_2O_4$) has been attracting attention due to its electronic, magnetic structure and catalytic properties [23].

As is well-known, Co_3O_4 (and in general all transition metal oxides) based catalysts are sensitive to water and will quickly

* Corresponding authors at: Research Institute of Applied Catalysis, School of Chemical and Environmental Engineering, Shanghai Institute of Technology, Shanghai 201418, China. (G. Lu).
E-mail addresses: houjinhuang@sit.edu.cn (H. Huang), gzhlu@ecust.edu.cn (G. Lu).

http://dx.doi.org/10.1016/j.jcat.2017.06.022
0021-9517/

deactivated by the presence of moisture in the gas stream [15,19,23]. The CO oxidation in moisture-rich conditions over the Co_3O_4 based catalysts was previously studied by several groups [2,15,19,24–26]. Grillo et al. [24] reported that the presence of moisture resulted easily in the carbonates formation, and thus depressed the catalytic activity of Co_3O_4. We have studied the deactivation mechanism of the Co_3O_4 catalyst by water with the DFT method [25], and found that there are three paths for the presence of water on Co_3O_4: H_2O dissociative adsorption in the O vacancies, H_2O dissociative adsorption on Co^{3+}, and H_2O molecular adsorption on Co^{3+}; and adsorbed CO could react with the OH group on the surface. Despite all this, water-induced deactivation of the catalysts, especially for the Co_3O_4-based catalysts, is still a challenging problem.

As illustrated above, the previous works focused mainly on the compositions and structures of the transition metal oxides themselves to improve the catalytic performance, aiming for stable operation. These efforts are almost ineffectual for solving the water vapor poisoning problem, because water molecules can occupy the catalytic active sites more readily than the reactant gases. Recently, to suppress the performance deterioration of transition metal oxide-based catalysts caused by water, the concept of hydrophobic coating for these catalysts was proposed and attempted, but the effectiveness is also minimal [3,27–29]. For example, Biemelt et al. synthesized amorphous carbon coated MnCu-based hopcalite nanoparticle catalysts by flame pyrolysis, and showed a certain level of water vapor resistance for CO oxidation, however, its catalytic activity decreased sharply (~50% loss) within only ~10 min, when being operated in a relative humidity of 75% (1.7 vol.% water, 20 °C) [28].

Herein, for the first time we designed a proper coating of gas-permeable vapor-resistant polymers, a layer of nanofilm, for the vapor-sensitive nanoparticles catalyst, to effectively improve its catalytic stability. The CoFe-based nanoparticles ($Fe_aCo_bO_x$) coated with hydrophobic polyester were prepared by the oxalic acid (OA)/ethlyene glycol (EG)-assisted solid-phase method, and their catalytic performance for CO oxidation under normal (3–10 ppm H_2O) and moisture-rich (~0.6 vol.% H_2O) conditions were investigated. The moisture-resistant characteristics of the catalysts and the effects of various preparation conditions, such as the Fe, Co, OA and EG amounts, as well as calcination temperature, etc., were also studied in detail. Based on these results obtained, the effects of material structures and chemical environments on the catalytic performances were discussed.

2. Experimental section

2.1. Catalyst preparation

The catalysts were prepared by a solid-phase method mediated with oxalic acid (OA)/ethlyene glycol (EG). In detail, $Fe(NO_3)_3{\cdot}9H_2O$ (≥98.5%), $Co(NO_3)_2{\cdot}6H_2O$ (≥99.0%) and $C_2H_2O_4{\cdot}2H_2O$ (OA, ≥99.0%) at designed ratios were weighed and put in an agate mortar at the room temperature. To facilitate the reaction and dispersion of this solid mixture, a measured amount of ethylene glycol was added. After hand grinding for 30 min, the sample was transferred to glass cup, ultrasonicated for 1 h, then dried at 110 °C overnight. Finally the sample was heated from the room temperature to the given temperature (200–400 °C) in air at 5 °C/min and kept at this temperature for 3 h. The prepared catalysts were referred to as $Fe_aCo_bO_x$-(OA_c-EG_d) (Fe/Co = a/b; OA/Co = c/b; EG/Co = d/b, mol).

2.2. Testing of the catalytic activity and kinetic data

The catalytic activities of the $Fe_aCo_bO_x$ catalysts for CO oxidation were examined at atmospheric pressure in a fixed bad quartz reactor (inner diameter 5 mm). In a typical experiment, 200 mg catalyst (40–60 mesh) and silica sand were added to the reactor. Before testing, the catalyst was pretreated at 200 °C in N_2 for 30 min. After cooling down to room temperature, the reactant gas of 0.15% CO and 18.9% O_2 balanced with N_2 was passed through the catalyst with weight hour space velocity (WHSV) of 15,000 mL/(g_{cat}·h). After stabilization for 10 min at given temperatures, the CO and CO_2 concentrations in the outlet gas stream were measured by an online gas chromatograph equipped with the nickel methanation furnace and hydrogen flame ionization detector (FID). Normal condition (3–10 ppm of H_2O) was obtained using the as-mixed normal feed gas. Moisture rich condition was obtained by passing the feed gas through an iced-water bubbler at 0 °C (~0.6 vol.% water vapor), and the concentration of water vapor was varied by adjusting the temperature of the water bubbler. CO conversion X(CO) was calculated by $X(CO) = 1 - C(CO)_{out}/C(CO)_{in} \times 100\%$, where $C(CO)_{in}$ and $C(CO)_{out}$ denote the concentrations of CO in the inlet and outlet, respectively.

The kinetic data was obtained in the same reactor as the catalytic activity testing. Based on the differential reactor mode, the CO conversion was controlled below 15%. The reactant gas consisted of 0.15% CO and 18.9% O_2 balanced with N_2 under normal condition (3–10 ppm of H_2O) and moisture rich condition (~0.6 vol.% water vapor). After steady operation for 30 min, the reaction rates were determined. The reaction rates r (mol/(g·s)) of CO was calculated by Eq. (1)

$$r\ (\mathrm{mol}/(\mathrm{g}\cdot\mathrm{s})) = (N_{CO} \times X(CO))/W_{cat} \quad (1)$$

where N_{CO} is the CO flow rate (mol/s), W_{cat} is the catalyst weight (g). When the CO conversion was <10%, the influence of the produced CO_2 and H_2O on the reaction rate (r) might be ignored. Hence, the empirical equation of the reaction rate for CO oxidation could be measured by Eq. (2).

$$r = A\exp\left(-\frac{E_a}{RT}\right)P_{CO}^{\alpha}P_{O_2}^{\beta} \quad (2)$$

$$\ln r = \ln A + \alpha \ln P_{CO} + \beta \ln Po_2 - E_a/RT \quad (3)$$

A is the pre-exponential factor, R is the ideal gas constant, T is the reaction temperature, P_{CO} is the partial pressure of CO and Po_2 is the partial pressure of O_2. In the process of kinetics data testing, the composition of the reactant gas remained essentially unchanged, and the CO conversion was <10% (1.3–8.8% under the condition of 3–10 ppm H_2O, and 1–8.5% under 0.6% H_2O), therefore, Eq. (3) can be simplified to Eq. (4). The activation energy (E_a) can be obtained from the slope of the resulting linear plot of ln r versus 1/T.

$$\ln r = -E_a/RT + C \quad (4)$$

2.3. Catalyst characterization

The surface area of the catalyst was measured on a Micrometrics ASAP 2020 M + C adsorption apparatus at −196 °C, and calculated by Brumauer–Emmett–Teller (BET) method. The X-ray powder diffraction (XRD) patterns were recorded on a PANalytical X'Pert Pro MRD X-ray diffractometer operated at 40 kV and 40 mA with Cu Kα radiation (λ = 0.154056 nm). The mean crystalline sizes (D) of Co_3O_4 and Fe_2O_3 in the catalysts were calculated by Scherrer equation, $D = \frac{\kappa\lambda}{\beta\cos\theta}$, where β is the broadening at half the maximum intensity (rad), κ is a dimensionless number (κ = 0.89), and θ is the Bragg angle. The X-ray photoelectron spectroscopy (XPS) spectra were obtained on a Thermo Scientific ESCALAB 250Xi with a monochromatized Al Kα X-ray source. All binding energies (BE) were determined with the C1s line (284.6 eV) of adventitious carbon. High-resolution transmission electron microscopy (HRTEM)

images were recorded on a Tecnai G^2 F20 S-TWIN (FEI Corporation) electron microscope operated at 200 kV. Thermogravimetric analysis (TGA) was performed on a Perkin Elmer Pyris Diamond TG/DTA Analyzer at a heating rate of 10 °C/min in air.

Hydrogen temperature-programmed reduction (H_2-TPR) of the catalyst was carried out in a continuous flow apparatus equipped with a TCD detector. 50 mg (40–60 mesh) of catalyst was used. Before testing, the catalyst was preheated at 200 °C in N_2 (50 mL/min) for 0.5 h to remove impurities and water adsorbed on the surface. The sample was then cooled to 50 °C followed by heating up to 700 °C at 10 °C/min in a gaseous mixture of 10% H_2/N_2 (50 mL/min).

Temperature-programmed desorption of CO (CO-TPD) and O_2 (O_2-TPD) on the catalyst was performed in a quartz tube reactor system equipped with a quadruple mass spectrometer (QMS, ICP 400, INFICON Co. Ltd.). 100 mg (40–60 mesh) of catalyst was used. Before testing, the catalyst was pretreated at 200 °C in pure He (30 mL/min) for 0.5 h, and then after cooled to room temperature in He, pure CO (30 mL/min) or O_2 (30 mL/min) was introduced into the catalyst bed and kept flowing for 1 h. After that, He (30 mL/min) was introduced instead of pure CO or O_2. CO-TPD (or O_2-TPD was run from room temperature to 680 °C at a rate of 10 °C/min, and the mass signals of CO (m/z = 28), CO_2 (m/z = 44) and O_2 (m/z = 32) were recorded.

The *in situ* diffuse reflectance infrared Fourier transform spectroscopy (DRIFTS) spectra were performed on a Nicolet 6700 FT-IR spectrometer equipped with an MCT detector at 70 °C. Before testing, the catalyst was pretreated at 200 °C in pure N_2 (50 mL/min) for 0.5 h, and then cooled to 70 °C to collect the background spectrum with a resolution of 4 cm^{-1} and a scan number of 64. After that, the reactant gases of 0.15% CO and 18.9% O_2 balanced with N_2 (50 mL/min) under both normal (3–10 ppm H_2O) and moisture rich condition (~0.6 vol.% H_2O) were flowed through the sample cell. The DRIFTS spectra were recorded at 70 °C. The FT-IR spectra were also recorded in a range of 400–4000 cm^{-1} on a Nicolet 380 FT-IR spectrometer at room temperature.

3. Results and discussion

3.1. Catalytic activity of $Fe_aCo_bO_x$ for CO oxidation

3.1.1. Effect of the Fe amount

The $Fe_aCo_bO_x$ sample was prepared with OA/Co = 1 and EG/Co = 0.5, and calcined at 350 °C. Effect of Fe amount on the catalytic activity of $Fe_aCo_bO_x$ is shown in Fig. 1. Fig. 1A shows that under normal condition with 3–10 ppm H_2O in the gas stream, the Co_3O_4 catalyst (without Fe) exhibited a rather high catalytic activity, and CO has been completely oxidized at as low as −78 °C. With the increase in the Fe content, the activity of $Fe_aCo_bO_x$ follow the form of a "volcano curve", that is, increased first, reached the peak platform and then decreased. When a/b = 3/16, the $Fe_3Co_{16}O_x$ catalyst shows the highest catalytic activities with −103 °C for T_{50} and −96 °C for T_{100}, ~12 °C (T_{50}) and ~18 °C (T_{100}) lower than those without Fe, respectively. The T_{50} and T_{100} values of all the catalysts are listed in Table 1.

For a comparison, the CO oxidation under moisture-rich condition (~0.6% H_2O) was also investigated. As shown in Fig. 1B, after adding ~0.6% moisture into the feeding gas stream, all the T_{100} values of the catalysts were greatly increased, and $Fe_3Co_{16}O_x$ still exhibited the best activity with a T_{50} value of 44 °C, about 30 °C lower than that without Fe. The activity of the $Fe_aCo_bO_x$ catalyst also increased with an increase in the Fe/Co ratio in the form of a "volcano curve", which is in consistent with the situation shown in Fig. 1A under normal condition (3–10 ppm H_2O). These results indicate that the presence of water and excessive amount of Fe in the $Fe_aCo_bO_x$ catalyst have negative effects on the catalytic activity, which are also in consistent with repeated results for Co_3O_4 [15,19,27,30] and Co ferrite [27] and Co-Al-Fe spinel [31]. While the negative effect of moisture on the catalytic activity of Co-based oxides is well known [15,19,23–25], the role of iron oxide in cobalt oxide matrix for CO oxidation has not been fully understood. As shown in Table 1, when Fe/Co was 3/16 (best for CO oxidation), the Co^{3+}/Co^{2+} ratio, the oxygen vacancies ($_vO$) and surface oxygen amount (O_s) reach maximum, and the content of lattice oxygen (O_L) reaches minimum, indicating that there are strong correlations between the Fe concentration in the Co oxide solid solution and the abundance/location of active oxygen species which may also associate with the Co^{3+}/Co^{2+} ratio. Our previous work has shown that addition of Fe to Co_3O_4 can increase its surface area, optimize the ratio of Co^{3+}/Co^{2+} on the catalyst surface, and promote CO adsorption and CO_2 desorption on the catalyst surface [20].

It is believed in this work that, some Fe-connected sol-like intermediate structures (precursors of metal oxides, such as Fe-O-(CH_2CH_2-O-COCOO-)$_n$), have been formed prior to the formation of solid-gel of Co-Fe oxide lattice. At the precursor with lower Fe amount, the calcination may not induce a segregation of the Fe species from the Co-matrix solid solution, and thus the higher the Fe:Co ratio, the higher the disorder of the Co-matrix (due to the fact that the radius of Fe^{3+} is larger than that of its Co counterpart), and the lower percentage of the lattice oxygen (O_L). When

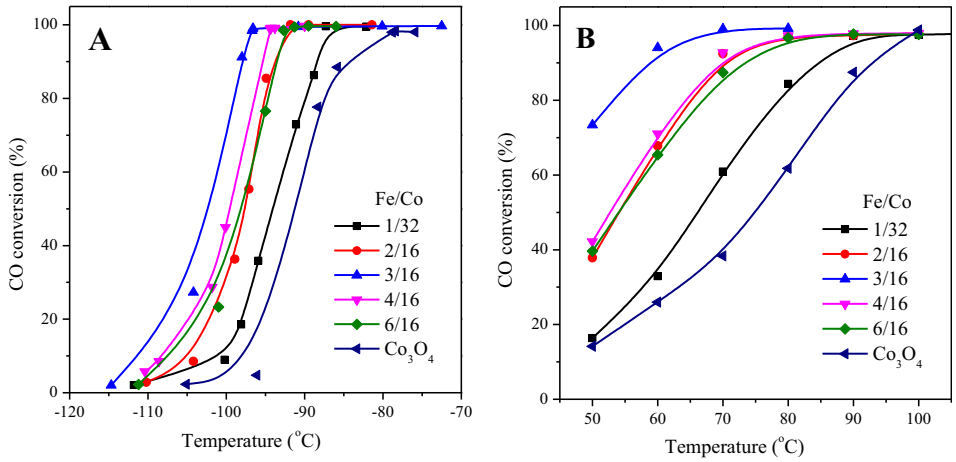

Fig. 1. The catalytic activity of the $Fe_aCo_bO_x$-OA_b-$EG_{b/2}$-350 catalyst with different Fe/Co ratio for CO oxidation in the presence of (A) 3–10 ppm H_2O and (B) ~0.6 vol.% H_2O. (Reaction conditions: 200 mg catalyst, reactant gas of 0.15% CO + 18.9% O_2/N_2 balanced with a flow rate of 50 mL/min.)

Table 1
Effects of the preparation factors and Fe amount on the catalytic activities (T_{50} and T_{100}), crystal sizes, BET surface areas (S_{BET}), BJH pore volumes and diameters of the $Fe_aCo_bO_x$ catalysts and their surface compositions obtained by XPS data.

$Fe_aCo_bO_x$-(OA_c-EG_d)			Calcined Temp. (°C)	T_{50} (°C)		T_{100} (°C)		Crystal size (nm)	S_{BET} (m^2/g)	Pore volume (cm^3/g)	Pore diameter (nm)	Co 2p	O 1s		
Fe/Co	OA/Co	EG/Co		3–10 ppm H_2O	0.6 vol.% H_2O	3–10 ppm H_2O	0.6 vol.% H_2O					Co^{3+}/Co^{2+}	vO (%)	O_S (%)	O_L (%)
Co_3O_4	1/1	1/2	350	−91	74	−78	100	24	36.9	0.22	9.6	1.01	10.8	19.5	69.6
0.5/16				−94	66	−87	90	18	58.2	0.24	6.5	1.06	11.4	20.4	68.2
2/16				−97	54	−91	80	20	50.2	0.24	7.6	1.13	12.3	21.8	65.9
3/16				−103	44	−96	70	21	49.8	0.23	7.5	1.32	14.8	22.0	63.2
4/16				−99	52	−94	80	22	44.6	0.25	9.0	1.23	13.8	19.9	66.3
6/16				−98	54	−92	90	23	41.4	0.24	9.7	1.01	12.2	17.5	70.3
Fe_2O_3												–	7.4	15.5	77.1
3/16	0	1/2	350	−90	71	−82	110	21	39.0	0.20	4.9	1.14	11.8	30.8	57.4
	1/2			−100	51	−95	80	22	40.2	0.21	8.3	1.21	12.5	25.1	62.4
	2/2			−102	44	−96	70	21	49.8	0.23	7.5	1.32	14.8	22.0	63.2
	4/2			−95	68	−93	100	23	38.0	0.22	9.2	1.02	10.7	33.9	55.4
3/16	1/1	0	350	−87	80	−81	110	24	41.2	0.22	8.2	1.20	8.3	29.5	62.2
		1/2		−102	44	−96	70	21	49.8	0.23	7.5	1.32	14.8	22.0	63.2
		2/2		−102	43	−97	70	19	50.5	0.25	8.1	1.42	16.2	16.9	66.9
		3/2		−97	46	−94	70	16	82.8	0.27	5.2	1.31	14.6	24.4	61.0
		4/2		−91	50	−85	80	15	61.5	0.25	6.3	1.06	11.1	28.0	60.9
3/16	1/1	1/1	200	−91	66	−87	100	15	95.4	0.21	5.1	0.84	5.3	55.6	39.1
			250	−114	47	−101	70	13	134	0.28	3.5	1.89	20.5	15.0	64.5
			300	−104	51	−98	80	18	64.2	0.26	6.6	1.76	17.8	15.9	66.3
			350	−102	53	−97	80	19	50.5	0.25	8.1	1.42	16.2	16.9	66.9
			400	−72	66	−46	90	29	24.9	0.20	12.4	1.30	4.6	24.4	71.0

the Fe/Co ratio reaches over a certain level (as Fe/Co > 3/16), with the increase in the Fe content, the segregation of the Fe species from the Co-matrix and further agglomeration (forming Fe_2O_3 nanocrystals eventually) become evident, which can be verified in the XRD spectra (Fig. S1A). These segregated Fe_2O_3 nanocrystals possess poorer catalytic activities and may also block the Co^{3+} active sites for CO oxidation.

3.1.2. Effect of the oxalic acid (OA) amount

In the preparation of $Fe_3Co_{16}O_x$ catalyst (with EG/Co = 0.5, and calcined at 350 °C), the effect of oxalic acid (OA) amount on its catalytic activity for CO oxidation is shown in Fig. 2. Under both the normal (3–10 ppm H_2O) and moisture-rich (~0.6 vol.% H_2O) conditions, T_{50} was decreased sharply initially with the increase in the OA amount and then increases gradually. When the ratio of OA/Co = 1 (mol), the catalyst exhibited the highest activity for CO oxidation, its T_{50} was −102 °C under normal condition and 44 °C under moisture-rich condition. And adding excessive OA in the preparation of catalyst has a negative effect, but its catalytic activity was still significantly higher than that without OA.

3.1.3. Effect of the ethylene glycol amount

Fig. 3 shows the catalytic activities of the $Fe_3Co_{16}O_x$ (OA/Co = 1, and calcined at 350 °C) catalysts with different amounts of ethylene glycol (EG). As shown in Fig. 3A, under normal condition (~3–10 ppm H_2O), T_{50} for CO oxidation was −87 °C over the catalyst without using ethylene glycol. After adding a small amount of EG (~6%wt., d:b = 1:2), T_{50} decreased sharply to −102 °C. With the increase in the amount of ethylene glycol, however, the activity of the catalyst followed the form of a "volcano curve". When EG/Co = 1/1 (mol), the catalyst showed the highest activity for CO oxidation, with T_{50} of −102 °C and 43 °C under normal and moisture-rich conditions, respectively. This result clearly shows that ethylene glycol is beneficial to the improvement of the

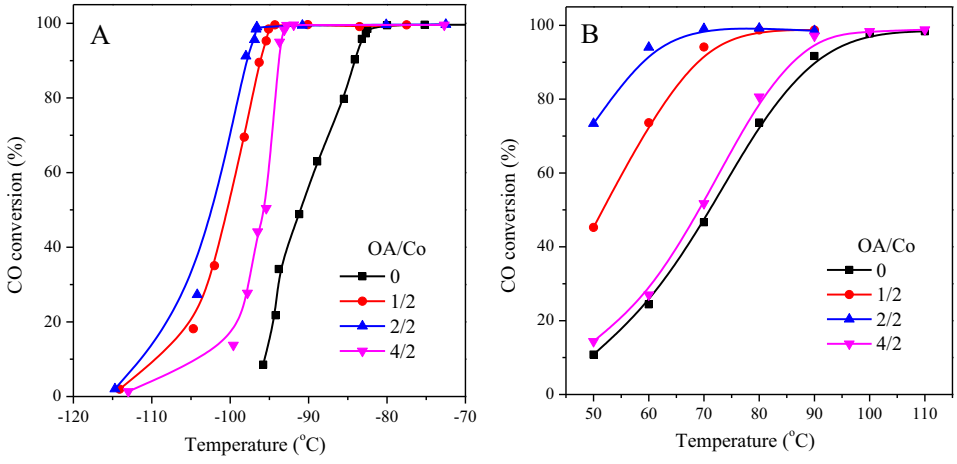

Fig. 2. The catalytic activity of the $Fe_3Co_{16}O_x$ catalyst prepared with different OA amounts for CO oxidation in the presence of (A) 3–10 ppm H_2O) and (B) ~0.6%vol H_2O. (Reaction conditions: 200 mg catalyst, reactant gas of 0.15% CO + 18.9% O_2/N_2 balanced with a flow rate of 50 mL/min).

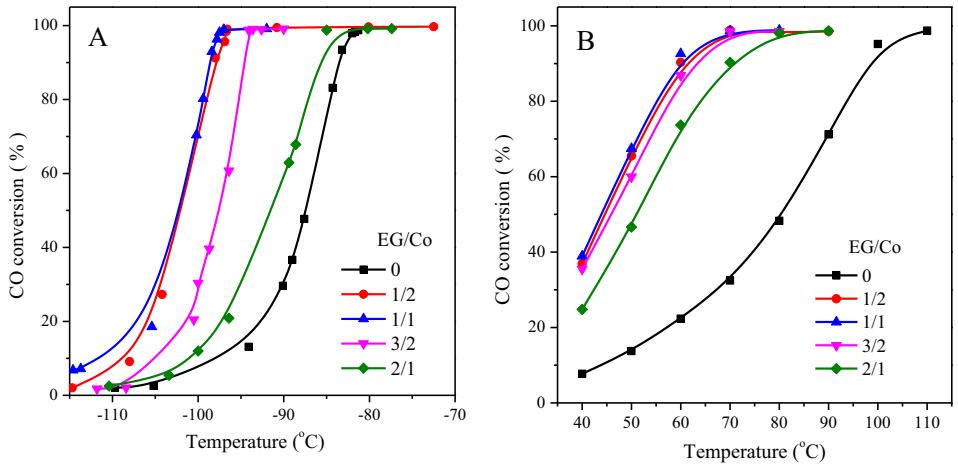

Fig. 3. The catalytic activities of the $Fe_3Co_{16}O_x$ catalysts prepared with different EG amounts for CO oxidation in the presence of (A) 3–10 ppm H_2O) and (B) ~0.6%vol H_2O. (Reaction conditions: 200 mg catalyst, reactant gas of 0.15% CO + 18.9% O_2/N_2 balanced with a flow rate of 50 mL/min).

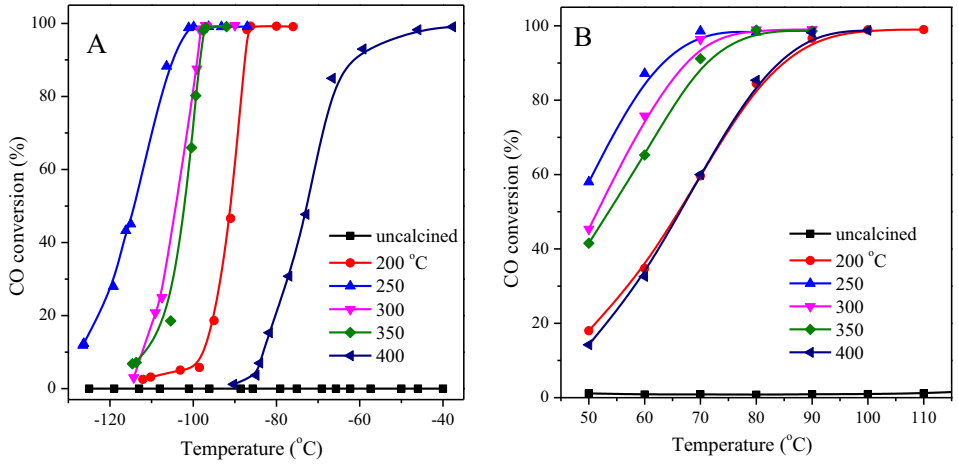

Fig. 4. The catalytic activities of the $Fe_3Co_{16}O_x$ catalysts calcined at 200–400 °C for 3 h for CO oxidation in the presence of (A) 3–10 ppm H_2O) and (B) ~0.6 vol.%H_2O. (Reaction conditions: 200 mg catalyst, reactant gas of 0.15% CO + 18.9% O_2/N_2 balanced with a flow rate of 50 mL/min).

catalytic activity. It was reported that ethylene glycol was used as a solvent for better dispersion and mixture of Co and Fe components [32–34], resulting in an improvement of the catalytic activity.

3.1.4. Effect of the calcination temperature

It is well known that the calcination temperature has a significant influence on the catalytic activity for CO oxidation [35]. The influence of the calcination temperature on the activity of the $Fe_3Co_{16}O_x$ (OA/Co = 1, and EG/Co = 1, mol) catalyst is shown in Fig. 4. The results show that the catalyst without calcination is almost inactive for CO oxidation in both conditions. With the increase in the calcination temperature (≥200 °C), the catalytic activities increased first then decreased, and the best catalytic activity can be obtained when the calcination temperature is 250 °C, with T_{50} of −114 °C and 47 °C under normal and moisture-rich conditions, respectively. Therefore, $Fe_3Co_{16}O_x$ (OA/Co = 1, and EG/Co = 1, mol) calcined at 250 °C was used the model catalyst in the following research works.

3.2. Catalytic stability and water resistance testing

The effect of water concentration on the CO conversion over the $Fe_3Co_{16}O_x$ catalyst is shown in Fig. 5. As shown in Fig. 5A, the $Fe_3Co_{16}O_x$ catalyst exhibit very high activity (100% conversion) in the whole range of 50–100 °C for CO oxidation under normal condition (3–10 ppm H_2O). When the reactant gas contained 0.6 vol.% H_2O, CO was completely converted at 70 °C. With the increase in the water vapor content, the CO conversion was obviously decreased, and T_{100} values shifted to higher temperature, which can be attributed to the competitive adsorption between CO and H_2O on the catalyst surface, and the active sites are blocked by the carbonates or H_2O/-OH species [16]. Interestingly, when the moisture level reached over 3.1 vol.%, T_{100} value remained almost the same (90 °C). This suggests that the $Fe_3Co_{16}O_x$ catalyst has a certain ability to resist water. The catalytic role of H_2O in CO oxidation was previously studied by several research groups [24,25,36–38]. Li et al. [11] and Gong et al. [38] found that the H_2O might affect the activation of oxygen and the decomposition of carbonate, and might provide a new reaction channel for CO oxidation with H_2O. Compared with the previous studies, the composition and structure in the catalyst might change the water adsorption equilibrium and provide a new reaction channel of CO oxidation under moisture-rich condition.

The catalytic stabilities of $Fe_3Co_{16}O_x$ operated at 90 °C and 70 °C under different water concentrations (0.6 vol.% and 3.1 vol.%) were examined, and the results are demonstrated in Fig. 5B. As we can see, the catalyst exhibited rather good stability for CO conversion even under moisture-rich condition. At 70 °C and with 0.6 vol.%

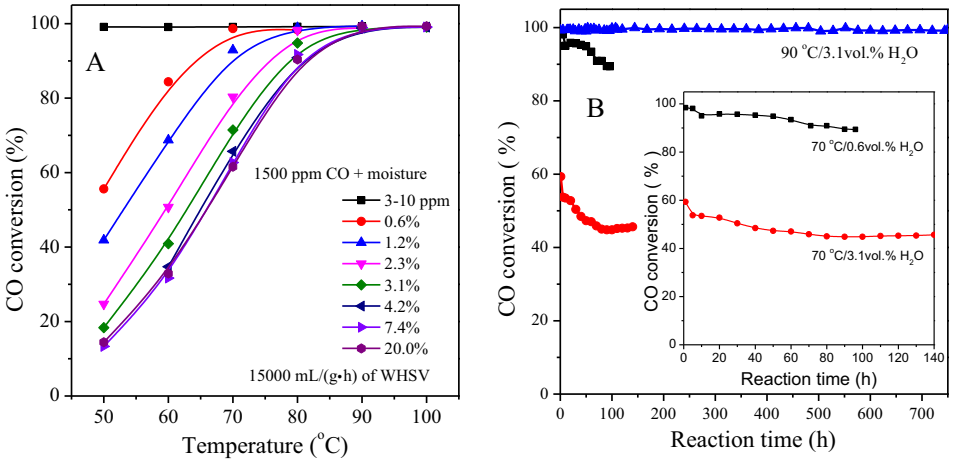

Fig. 5. Effect of H_2O concentration in the reactant gas on (A) the catalytic performance of $Fe_3Co_{16}O_x$ catalyst at 50–100 °C, and (B) its catalytic stability at 70 °C and 90 °C. (Reaction conditions: 200 mg catalyst, reactant gas of 0.15% CO + 18.9% O_2/N_2 balanced with a flow rate of 50 mL/min).

H_2O in the reactant gas, the 100% CO conversion initially was obtained, then it tended to deteriorate gradually and but still remained >90% CO conversion after 96 h of the reaction. When the moisture level was raised to 3.1 vol.%, the CO conversion dropped to ~60% in the first 1 h, and then gradually declined to ~47% after 60 h operation, and finally stabilized at ~45% conversion after 70 h, which means that 75% of the catalytic activity was kept and remained stable (stopped observation at 145 h). Remarkably, when the reaction was operated at 90 °C, no deactivation of this catalyst could be observed for over one month (100% conversion, stopped observation at 750 h), even with 3.1 vol.% H_2O in the reactant gas.

For the cobalt-based catalysts for CO oxidation, water vapor is the key deteriorating factor [19,26,39,40]. Xie et al. studied the catalytic stability of Co_3O_4 nanorods under different conditions and showed that the catalyst could keep 100% CO conversion at room temperature for 65 h under normal condition (3–10 ppm H_2O), and only 90% CO conversion at 150 °C under moisture-rich condition (8.2 vol.% H_2O) after 10 h of the reaction [15]. Song et al. prepared mesoporous Co_3O_4, which could achieve 100% CO conversion at 80 °C under moisture-rich condition 3 vol.% H_2O initially, and after 24 h of the reaction at 100 °C the CO conversion was decreased from 100% to 50%; when the reaction temperature was increased to 150 °C, only 100% CO conversion was kept for 24 h [19]. Xu et al. investigated the water tolerance of Co_3O_4, and found that adding 5% water vapor into the reaction feed made the CO conversion sharply decrease from 100% to 40% in the initial 3 h at 100 °C [26]. Kuo et al. synthesized F-Co_3O_4@CNT catalyst, and found that 100% CO conversion was obtained over this catalyst under 3 vol.% H_2O condition for 26 h but only at as high as 150 °C [3]. Compared with these results, the $Fe_3Co_{16}O_x$ catalyst prepared in this work shows much improved stability and water resistance, even though the operation conditions are varied from case to case.

3.3. Reaction kinetics of CO oxidation over the nanofilm-coated catalyst

In this work, we have achieved the CO oxidation with unprecedented durability at relatively low temperature (70 °C) under moisture-rich condition (3.1 vol.%) using low-cost Co-Fe oxide as the catalyst. 100% CO conversion has also been obtained at 70 °C under a moisture level of 0.6 vol.% These achievements can be attributed to two folds: the optimization of various synthetic conditions and the polymer nanofilm coating for this $Fe_3Co_{16}O_x$ catalyst.

The influence of the reaction conditions (CO concentration and WHSV) on CO oxidation over the $Fe_3Co_{16}O_x$ catalyst was tested under normal and moisture-rich conditions, and the results are shown in Fig. 6(A–C). As can be seen, the catalyst exhibited generally better CO conversion at lower CO concentration under both conditions, and this shows that it is much more sensitive to CO concentration for the catalyst operated under moisture-deficit than under moisture-rich condition, indicating that there are different conversion rate-limiting factors in these two cases.

It is understandable that high CO concentration has a negative influence on the CO conversion when the supply of active oxygen is not enough for matching the consumption of the adsorbed CO [32]. In addition, CO_2 may also play an important role in the catalytic activity [41,42], since carbonates remain on the surface and cover the active sites for CO adsorption and reaction. The competitive adsorption among CO, H_2O and CO_2 on the catalyst surface may be another reason for the decrease in the CO conversion.

The effect of the weight hour space velocity (WHSV) was also investigated over the $Fe_3Co_{16}O_x$ catalyst, and the results are shown in Fig. 6C. When WSHV was below 15,000 mL/(g_{cat}·h), the CO conversion was hardly influenced at 30–80 °C, that is to say, the decrease of WHSV below a certain level could not enhance the CO conversion in the presence of 0.6 vol.% H_2O in the reactant gas. When WHSV was higher than the threshold, the reaction temperature for achieving the same CO conversion shifted higher. This result is in consistent with the effect of CO concentration with 0.6 vol.% water vapor (Fig. 6B).

Fig. 6D shows Arrhenius plots for the rate of CO oxidation over the polymer nanofilm-coated CoFe oxide ($Fe_3Co_{16}O_x$) catalyst at different moisture levels. The apparent activation energy (E_a) of CO oxidation is 22.0 kJ/mol under normal condition (3–10 ppm H_2O), which is comparable with those of the uncoated Co-based oxides repeated [15,32,33], implying that a similar reaction pathway for CO oxidation is presented. Xie et al. [15] suggested that naked Co_3O_4 nanorods and Co_3O_4 nanoparticles have the identical kind of active sites (Co^{3+} ions) for CO oxidation, which may also be the active sites for our coated system in term of the similar value of E_a. Under moisture rich condition (0.6 vol.%), E_a reached 55.6 kJ/mol, much higher than that under normal condition (3–10 ppm), suggesting that reaction rate-determining step may have been substantially changed due to the presence of water vapor.

The reaction rates TOF values over the $Fe_3Co_{16}O_x$ catalyst at 30–60 °C under both moisture rich (0.6 vol.%) and normal conditions are listed in Table 2, which fall into the range of 5.0–39.9 × 10^{-8} mol/(g·s). While the comparison is somewhat arbitrary, it is still striking to note that the polymer nanofilm coated CoFe catalyst

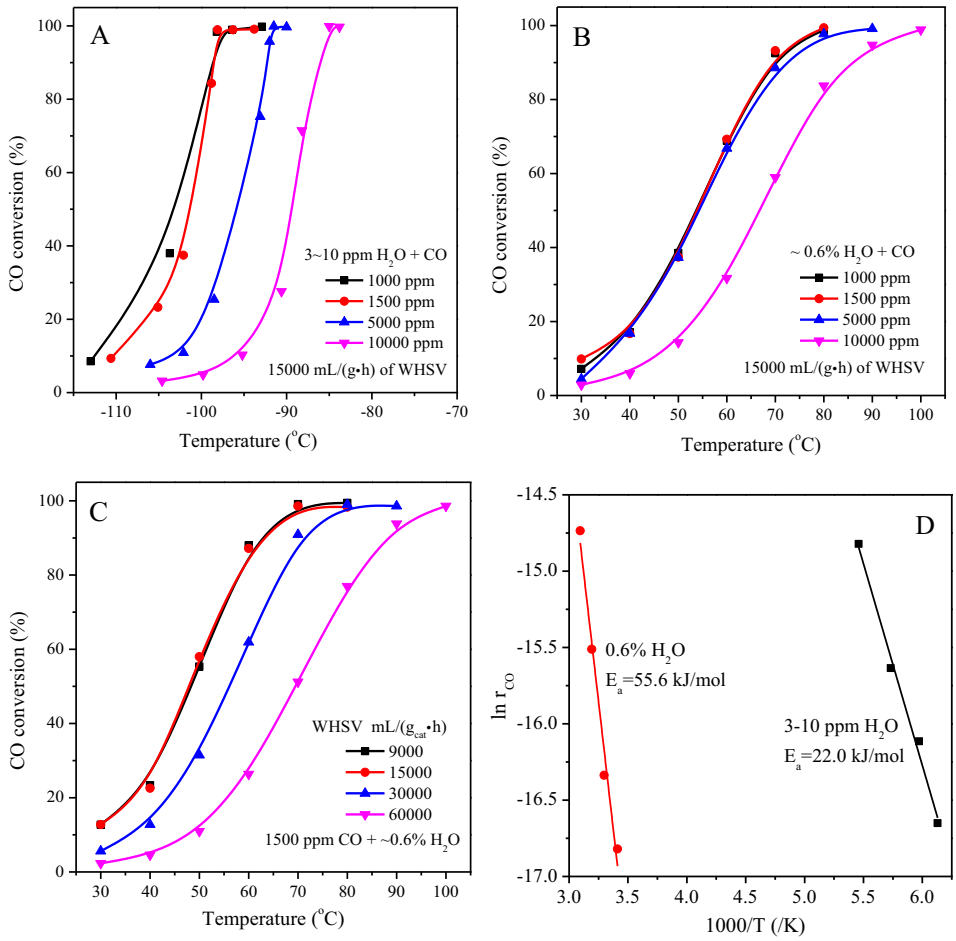

Fig. 6. The effect of CO concentration (0.5%O_2/N_2 balanced) on the CO conversion with (A) 3–10 ppm H_2O and (B) 0.6 vol.% H_2O; (C) The effect of WHSV on the CO conversion (18.9%O_2 + 0.15%CO + 0.6 vol.% H_2O/N_2 balanced); (D) Arrhenius plots of ln r_{CO} versus 1000/T for CO oxidation over the $Fe_3Co_{16}O_x$ catalyst (1500 ppm CO/air with ~0.6 vol.% or 3–10 ppm moisture).

Table 2
Reaction rates (r) of CO oxidation over the $Fe_3Co_{16}O_x$ catalyst and their TOF values.

Temperature T_1 (°C)	$r_1 \times 10^8$ (mol/g.s, 0.6 vol.%H_2O)	TOF $\times 10^{10}$ (mol/s·m^2)	Temperature T_2 (°C)	$r_2 \times 10^8$ (mol/g·s, 3–10 ppm H_2O)	TOF $\times 10^{10}$ (mol/s·m^2)
30	5.0	3.7	−110	5.9	4.4
40	8.0	6.0	−106	10.0	7.4
50	18.4	13.7	−98	16.2	12.1
60	39.9	29.8	−90	36.6	27.3

presented for the first time is more active than some noble metal (Pd, Pt, and Au) catalysts for CO oxidation under moisture rich condition. For instance, the reaction rate over this catalyst at 50 °C is 18.4×10^{-8} mol/(g·s), which is higher than those over Pt/TiO_2 (14×10^{-8} mol/(g·s)) at 27 °C, and Au/Fe_2O_3 (3.8×10^{-8} mol/(g·s)) at 27 °C [43].

3.4. Characterization of structural and physicochemical properties

3.4.1. XRD

Effect of the preparation factor and Fe amount on the XRD patterns and crystal sizes of the Fe_aCo_bOx catalysts are shown in Fig. S1 and Table 2, in which the crystal sizes were calculated by Scherrer Equation. In the XRD pattern of Fe_2O_3 (Fig. S1A), both hematite (α-Fe_2O_3, JCPDS 33-0664) and maghemite (γ-Fe_2O_3, JCPDS 39–1346) can be found, and for pure Co_3O_4, only the spinel structured cobalt phase (JCPDS 43-1003) can be found. After doping with low concentration of Fe (Fe/Co < 3/16), no diffraction peaks of hematite (α-Fe_2O_3) or maghemite (γ-Fe_2O_3) can be observed, indicating that Fe species are well-dispersed in Co_3O_4. When increasing Fe/Co to 3/16, the weak diffraction peaks of Fe_2O_3 can be identified, implying that Fe_2O_3 nanocrystals start to form and segregate from the Co_3O_4 host lattice. This is in consistent to the highest Co^{3+}/Co^{2+} ratio, the highest percentages of vacancy oxygen ($_vO$) and surface oxygen species (O_S) and lowest level of lattice oxygen (O_L), as seen in Table 1, as well as to the optimal catalytic activity for CO oxidation when Fe/Co = 3/16.

As is well-known, the calcination has a significant influence on the physicochemical property of the catalyst [44,47]. For the $Fe_3Co_{16}O_x$ catalyst, the uncalcined sample showed a mixed phase of $C_2CoO_4{\cdot}2H_2O$ (JCPDS 25-0250) and $C_2FeO_4{\cdot}2H_2O$ (JCPDS 22-0635), and the samples calcined at 200–400 °C have a typical pattern of spinel Co_3O_4 (Fig. S1D). Increasing the calcination temperature (200–400 °C) results in sharper diffraction peaks, and the diffraction patterns of Fe_2O_3 start to emerge at 350 °C and become more evident at 400 °C for the $Fe_3Co_{16}O_x$ catalyst.

The average particle size was ~19 nm after this catalyst was calcined at 350 °C, while its size reduced to ~13 nm when calcined at 250 °C. Further decreasing the calcination temperature did not produce smaller particles (~15 nm). During the preparation of the catalyst, the particle size decreased (from 24 nm to 15 nm) almost linearly with the increase in the ethlyene glycol (EG) amount, and this effect was not seen when oxalic acid (OA) was added, suggesting that the formation of polyester nanofilm restricts the growth of catalyst nanocrystals. The smallest average particle size (~13 nm) formed when the calcination temperature is 250 °C for the catalyst $Fe_3Co_{16}O_x$ (OA/Co = 1, and EG/Co = 1, mol), which is also the catalyst showing the best catalytic activity and stability.

3.4.2. TEM and TG analysis

As shown in TEM image (Fig. 7A), the $Fe_3Co_{16}O_x$ particles are almost all smaller than 30 nm with an average diameter of 11.3 nm, slightly smaller than 13.0 nm measured by Scherrer Equation. And the nanoparticles appear to have various morphologies: elliptical, spherical, and irregular shape. Interestingly, many of these nanoparticles are coated with a thin layer of organic materials which are very different from the metal oxide core (Fig. 7B and C). The thickness of the polymer coating layer is in the range of 0.3–2 nm, and the total organic content is about 1.8 wt.% measured by the weight loss in the thermogravimetric analysis at 250–700 °C (Fig. 7D). The average thickness of the polymer nanofilm estimated from the average particle size (13 nm) of the metal oxide core and the weight percentage of the organic shell is 0.25 nm after taking account of the densities of the core (~6.0 g/cm^3) and the shell (~0.9 g/cm^3), which is significantly smaller than the thickness observed by the TEM image. This discrepancy may originate from the fact that some nanoparticles tend to form large aggregates on which only the outermost particles are coated with the nanofilm. If we consider all the weight loss above 100 °C in TGA resulted from the organic materials, the thickness of the nanofilm shell would become 0.33 nm, which is in reasonable consistent with that observed in TEM images.

It should be pointed out that, since the sample prepared for TEM observation was through dispersion by ultrasonication in ethanol, the actual thickness of the coating layer may be different from that observed. Considering that ethanol is a good solvent for the polymers coated in this $Fe_3Co_{16}O_x$ catalyst, such as polyethylene oxalate synthesized from OA and EG, we tentatively assume that there exist strong interactions, such as chemical bonds, like —CoFe—O—(CH_2CH_2—O—COCOO—)$_n$, between the coating polymer molecules and the core metal oxides. While this assumption is still in a preliminary stage and worthy further study, this tightly coating nanofilm layer may be critical in isolating water molecules from the coated metal oxides and further preventing the formation of carbonates that can deactivate the metal oxide catalyst completely.

To study the thermal properties of the coating polymer, the $Fe_3Co_{16}O_x$ catalyst calcined at 250 °C was heated programmedly in air or N_2. The results (Fig. S2) show that CO_2 with a small quantity of CO were detected in air atmosphere, and only CO_2 was observed in N_2 atmosphere. As shown in the FT-IR spectra (Fig. S3), in the

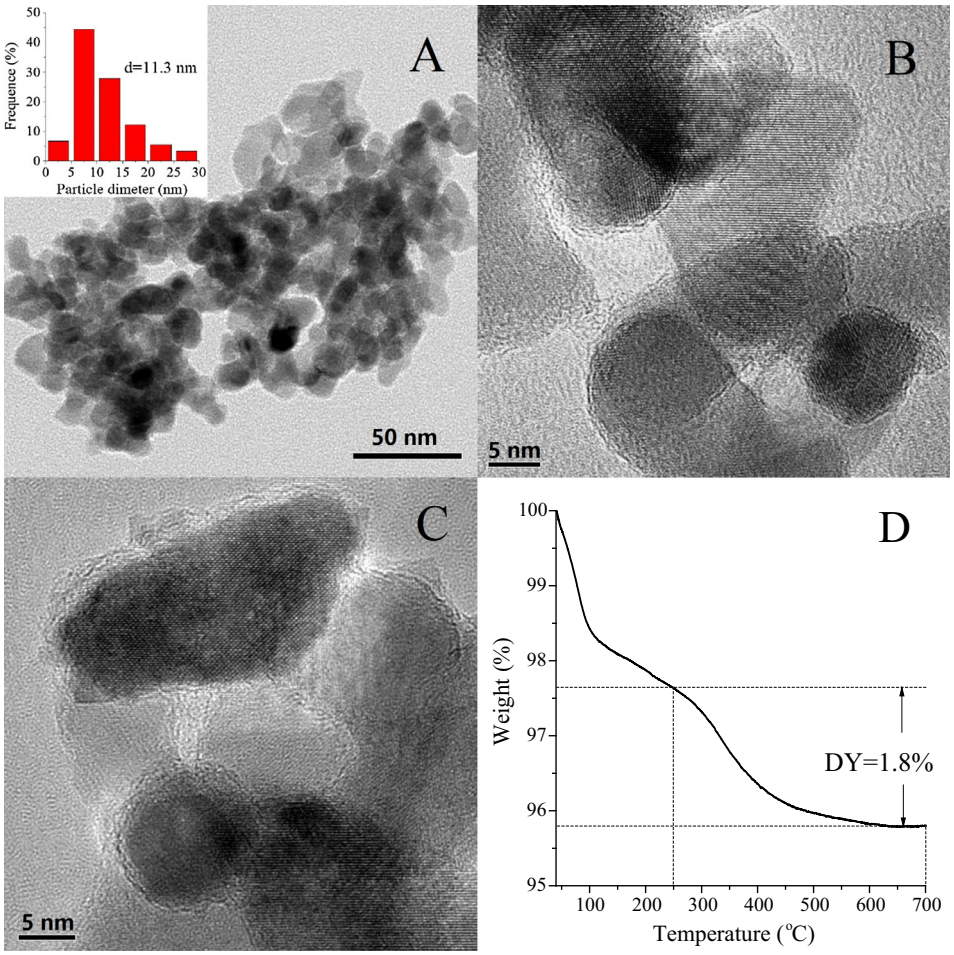

Fig. 7. (A–C) HRTEM images and (D) TG curve of the polymer nanofilm-coated CoFe oxide nanoparticles ($Fe_3Co_{16}O_x$).

sample without calcination, there are the IR absorption peaks of —CH_2—, —CH_3 groups, oxalate (O_x^{2+}) and carbonate species; after being calcined at >250 °C, these IR absorption peaks decreased obviously and some peaks have disappeared, indicating the decomposition of carbonate and oxalate species. For the catalyst calcined at 400 °C, however, the IR absorption peaks of OH groups on the carboxyl species at 1630 cm^{-1} and —CH_2—, —CH_3 groups at ~1388 cm^{-1} can still be found. These results show that the presence of the coating polymer (—(CH_2CH_2—O—COCOO—)$_n$) on the catalyst surface and the decomposition of carbonate and oxalate species after calcination.

3.4.3. N_2 adsorption–desorption

The BET surface areas (S_{BET}), BJH pore volumes and diameters of the $Fe_aCo_bO_x$ catalysts obtained by N_2 adsorption–desorption experiments are given in Table 2. The results show that S_{BET} increased first and then decreased along with the amount of Fe, OA and EG. And also with the increase in the calcination temperature from 200 °C to 400 °C, S_{BET} increased first and then decreased, showing that the catalyst calcined at 250 °C has the highest surface areas (134 m^2/g), the largest pore volumes (0.28 cc/g) and the smallest pore diameter (3.5 nm). And that higher S_{BET} is beneficial to supplying more active sites for CO adsorption and weakening the bond strength of Co—O [19,48], and the S_{BET} data shown in Table 2 are generally in consistent with the catalytic activities of the catalysts.

The N_2 sorption isotherms of the $Fe_3Co_{16}O_x$ catalyst and BJH desorption pore size distributions of the $Fe_3Co_{16}O_x$ catalysts calcined at different temperature are shown in Fig. 8. As shown in Fig. 8A, the $Fe_3Co_{16}O_x$ catalyst calcined at 250 °C appears to be a typical IV-type adsorption isotherm, implying that there exists a regular mesoporous structure [49]. And its most probable pore diameter is lower than those calcined at other temperatures (Fig. 8B), and their most probable pore diameter can be ranked in the order of the sample-250 (calcined at 250 °C, 3.71 nm) < 200 (5.5–7.0 nm) < 300 (7.88 nm) < 350 (9.40 nm) < 400 (11.6 nm).

3.4.4. XPS

The surface properties, such as surface composition and chemical valence states, play an important role in understanding the performance and reaction mechanism of the catalyst [50,51]. The XPS spectra of the $Fe_aCo_bO_x$ catalysts are shown in Fig. S4. For all the $Fe_aCo_bO_x$ catalysts, the Co $2p_{3/2}$ and Co $2p_{1/2}$ peaks are observed at around 780 and 795 eV respectively, indicating the existence of Co_3O_4 [22,51,52]. The Co 2p spectra were further deconvoluted into Co^{2+} (781.3 and 796.5 eV), Co^{3+} (779.8 and 795.0 eV) and Co^{2+} satellite peak (787.1 and 803.9 eV) signals, respectively (Fig. S4A) [21,23,33,52,53]. The atomic ratios of Co^{3+}/Co^{2+} on the surface of the $Fe_aCo_bO_x$ catalysts calculated from the corresponding peak areas are listed in Table 1.

On the surface of the $Fe_aCo_{16}O_x$-(OA_{16}-EG_8) catalysts calcined at 350 °C, the atomic ratio of Co^{3+}/Co^{2+} first increased and then decreased with increase in the Fe amount. When Fe/Co = 3/16, the Co^{3+}/Co^{2+} ratio reached the highest (1.32) (Fig. 4S A1). With increasing the amount of OA and EG, and the Co^{3+}/Co^{2+} atomic ratios also were changed in form of a volcano curve, and when OA/Co or/and EG/Co was 1/1, the Co^{3+}/Co^{2+} ratio reached the highest, which is in consistent with the activities of the catalysts (Fig. 4S A2 and A3). For the catalysts calcined at different temperatures, after calcination at 200 °C the Co^{3+}/Co^{2+} atomic ratio was 0.84, much lower than other catalysts calcined at higher temperatures, e.g. 1.89 for the sample calcined at 250 °C, due to the incomplete decomposition of the oxalate (Fig. 4S A4). However, further increase in a calcination temperature may induce the decreases of oxidative oxygen species in oxygen vacancies ($_vO$) and on surface (O_s), and thus the Co^{3+}/Co^{2+} atomic ratio is suppressed.

The O 1 s spectra were deconvoluted into three oxygen species (Fig. S4B). The peak at ~529.9 eV was attributed to the lattice oxygen (O_L, such as Co—O or Fe—O) [19,55], the peak at ~531.1 eV was attributed to the surface oxygen (O_S, such as OH^-, O_2^- or O^-) [47,56], and the peak at 532.1 eV was attributed to the oxygen vacancies or defective oxygen (vO) [19,57]. As shown in Fig. S2B1, compared with the pure Co_3O_4 and Fe_2O_3, the O_L peaks of the $Fe_aCo_{16}O_x$-(OA_{16}-EG_8) catalysts calcined at 350 °C are shifted slightly toward a higher binding energy, which suggests that adding Fe to Co_3O_4 may change the chemical environment of O and increase the oxygen vacancies (Table 2) on the surface. Peak area percentages of O_L, O_S and vO are listed in Table 1. Note that vO content increased first and then decreased with adding Fe content, which is conformed with the catalytic activities. Similar changing trends of vO content can be found by changing the content of OA or ethylene glycol or the calcination temperature (Fig. S4(B2-B4)). It is worth noting that O 1s of the $Fe_3Co_{16}O_x$-(OA_{16}-EG_{16}) catalyst calcined at 200 °C is much different from the catalysts calcined at other temperatures, i.e., the peak around 531.8 eV, which is assigned to the incomplete decomposition of $C_2O_4^{2-}$, has much high area than those of other catalysts. The highest amount of oxygen vacancies (20.5%) is observed on the surface of the $Fe_3Co_{16}O_x$ catalyst calcined at 250 °C.

3.4.5. H_2-TPR

The reduction behavior and oxygen storage capacity of the catalyst can be obtained by the help of H_2-TPR, and the H_2-TPR profiles of the $Fe_aCo_bO_x$ catalysts are shown in Fig. 9. For the pure

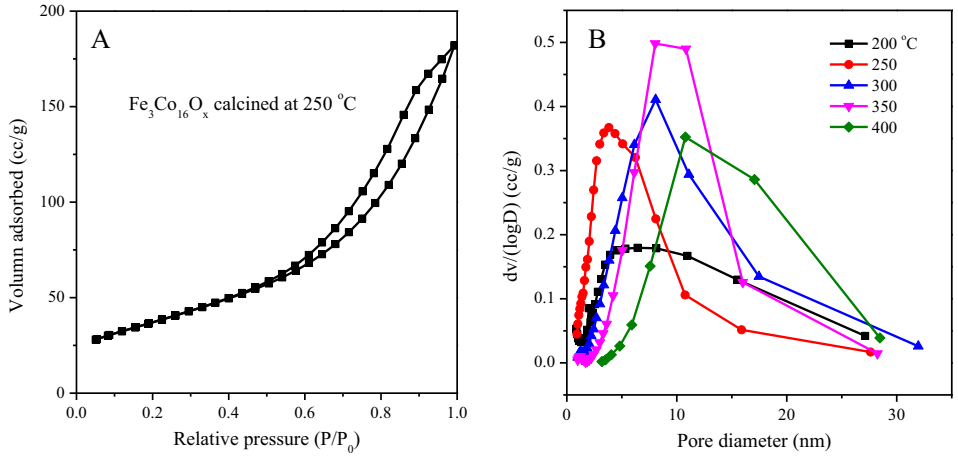

Fig. 8. (A) N_2 sorption isotherms of the $Fe_3Co_{16}O_x$ catalyst calcined at 250 °C and (B) BJH desorption pore size distributions of the $Fe_3Co_{16}O_x$ catalyst calcined at 200–400 °C.

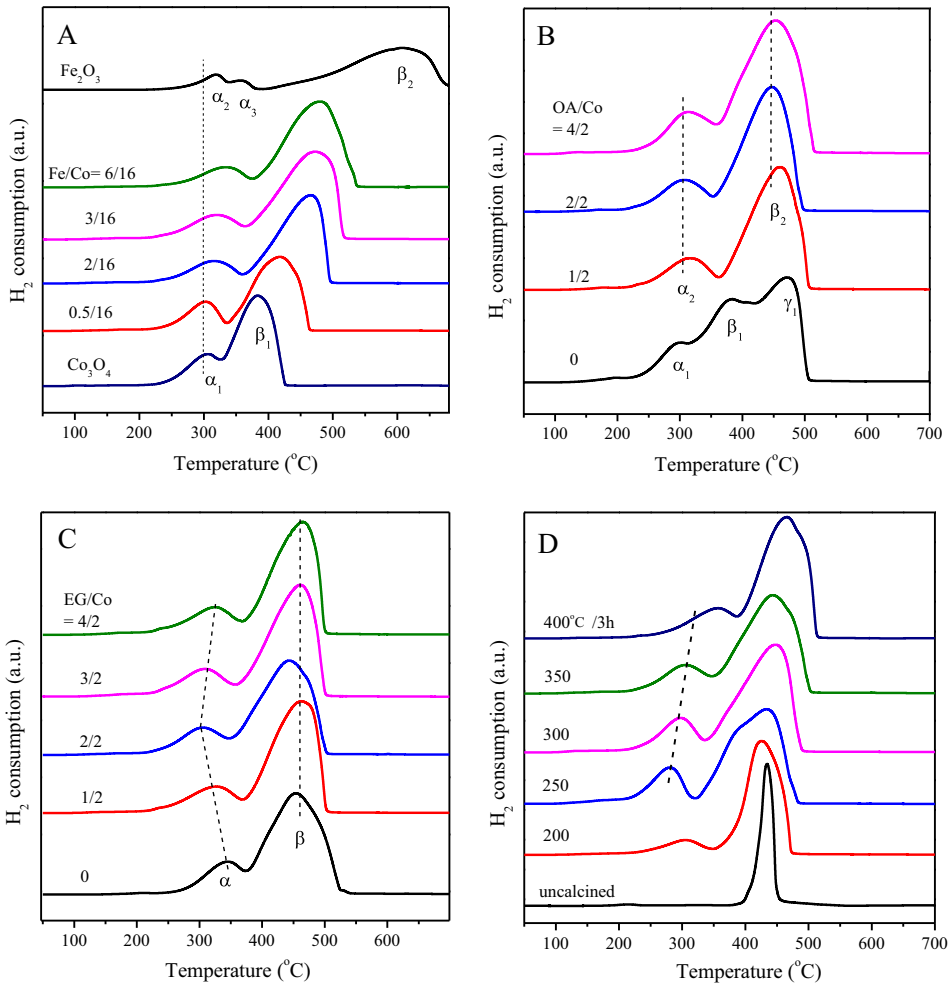

Fig. 9. H_2-TPR profiles of (A) $Fe_aCo_bO_x$-(OA_b-$EG_{b/2}$, 350 °C) with different Fe/Co; (B) $Fe_3Co_{16}O_x$-(EG_8, 350 °C) with different OA/Co; (C) $Fe_3Co_{16}O_x$-(OA_{16}, 350 °C) with different EG/Co; (D) $Fe_3Co_{16}O_x$-(OA_{16}-EG_{16}) calcined at different temperatures.

Fe_2O_3 (Fig. 9A), three reduction peaks are observed and correspond to the reduction of γ-Fe_2O_3 to Fe_3O_4 (α_2), α-Fe_2O_3 to Fe_3O_4 (α_3) and Fe_3O_4 to Fe^0 (β_2), respectively [58]. This is in consistent with the XRD pattern of Fe_2O_3 which consists of α-Fe_2O_3 and γ-Fe_2O_3, and also suggests that γ-Fe_2O_3 is easier to be reduced than α-Fe_2O_3. For the pure Co_3O_4, its reduction is a two-step processes of $Co_3O_4 \rightarrow CoO \rightarrow Co^0$ [19,50,59,60], which are corresponding to the low-temperature peak (α_1) and high-temperature peak (β_1), respectively. After doping Fe into Co_3O_4, the α_1 peak shifts slightly to higher temperature and the β_1 peak moves to much higher temperature (as 375 → 465 °C for $Fe_3Co_{16}O_x$), which is in agreement with the results reported [44,45]. Based on the detailed XPS results in Table 1, the reduction of cobalt oxide by hydrogen may be hindered by the presence of oxidative species, such as chemically bonded reactive surface oxygen. The higher the quantity of the oxidative species (the highest for $Fe_3Co_{16}O_x$), the more difficult the reduction of the catalyst by hydrogen is. In addition, the presence of iron oxide and the strong interaction between Co and Fe oxides may complicate the situation, since iron oxide is more difficult to be reduced by hydrogen.

As shown in Fig. 9B, the catalyst prepared without using OA showed three reduction peaks (α_1, β_1, γ_1), which can be ascribed to the reduction of Co_3O_4 ($Co_3O_4 \rightarrow CoO \rightarrow Co^0$) and Fe_2O_3, respectively. After using OA in the preparation of catalyst, these three peaks merged into two peaks, and the catalyst with OA/Co = 1/1 showed the lowest reduction temperature. As shown in Fig. 9C, the reduction profiles of the catalysts prepared with ethylene glycol were similar to the one without ethylene glycol, and with increasing the ethylene glycol amount, both reduction peaks shifted to lower temperature initially and then shifted to higher temperature. When the catalyst was prepared with EG/Co = 1/1 the reduction temperature of its two peaks were the lowest. These results are in accordance with their catalytic activities, that is, the easier the reduction the higher the catalytic activity is [19].

The effect of the calcination temperature on the reducibility of the catalyst is shown in Fig. 9D. The results show that the catalyst without calcination showed a narrow reduction peak around 440 °C originated from both C_2FeO_4 and C_2CoO_4. After calcination at 200 °C, a small reduction peak around 300 °C appeared. The lowest-temperature reduction peak occurred when the catalyst was calcined at 250 °C. When the calcination temperature was at >250 °C, the reduction peaks shifted to higher temperature, and the higher the calcination temperature the higher the reduction temperature of two peaks was, which suggests that higher temperature calcination leads to formation of larger particles (from XRD), resulting in lower reducibility of the catalyst.

3.4.6. CO-TPD and O_2-TPD

After CO was adsorbed on the $Fe_aCo_bO_x$ catalysts, their CO_2 desorption curves in absence of O_2 are shown in Fig. 10. As shown in Fig. 10A, in the CO_2-TPD curve of pure Co_3O_4, there are three CO_2 desorption peaks (α, β, γ), which can be attributed to the adsorbed

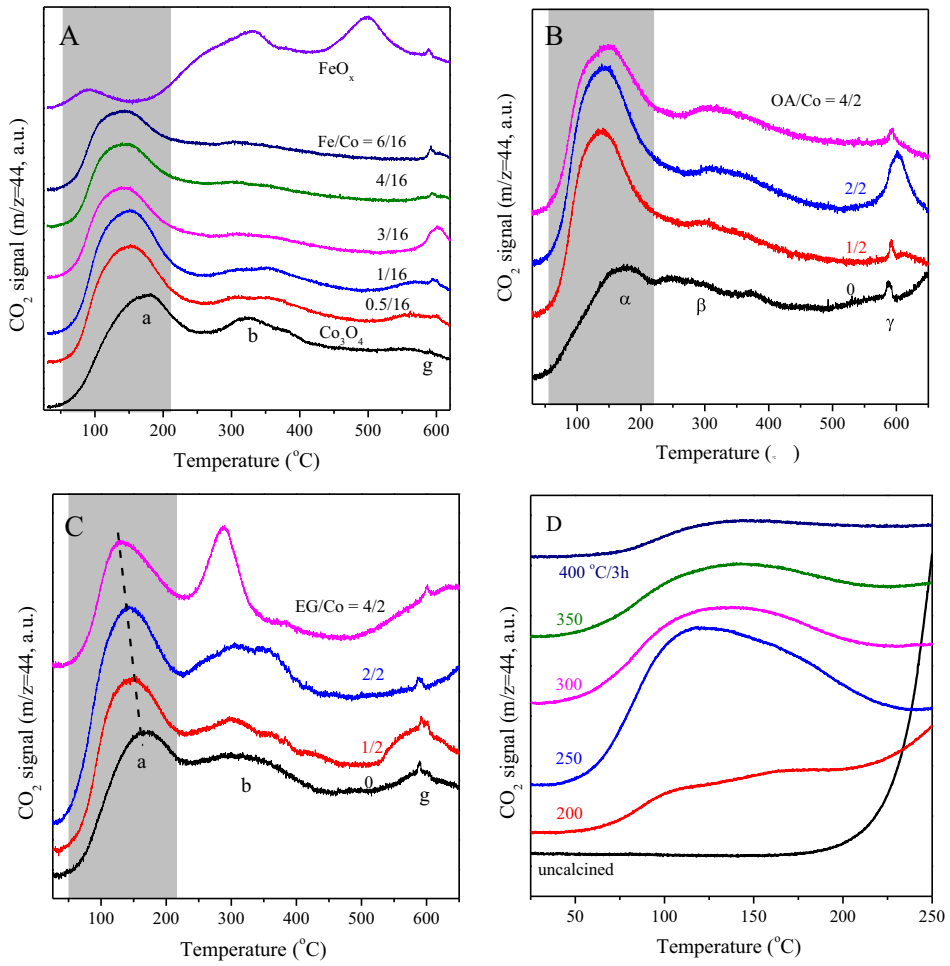

Fig. 10. CO_2-TPD profiles of (A) $Fe_aCo_bO_x$-(OA_b-$EG_{b/2}$, 350 °C) with different Fe/Co, (B) $Fe_3Co_{16}O_x$-(EG_8, 350 °C) with different OA/Co, (C) $Fe_3Co_{16}O_x$-(OA_{16}, 350 °C) with different EG/Co, and (D) $Fe_3Co_{16}O_x$-(OA_{16}-EG_{16}) calcined at different temperatures, after CO adsorption.

CO reacted with the superficial oxygen species, the vacancy-related oxygen and the lattice oxygen, respectively [20,41]. With the increase in the Fe doping in Co_3O_4, the α peak shifted to lower temperature, which implies that the superficial oxygen species on the catalyst become more reactive with the adsorbed CO. However, the CO_2 desorption peaks from pure Fe_2O_3 are very much different from those from the $Fe_aCo_bO_x$-(OA_b-$EG_{b/2}$, 350 °C) or Co_3O_4 catalysts.

For the $Fe_3Co_{16}O_x$ catalyst, when OA was not used in preparation of the catalyst, its area of CO_2 (α) desorption peak is much smaller than those of the catalysts prepared with OA (Fig. 10B), indicating that its content of the superficial oxygen species is much smaller than those prepared with OA. Li et al. suggested that only the low-temperature peak (α) played a crucial role in CO oxidation, and other two peaks (β, γ) were not relevant to the CO catalytic activity [20]. Further, increasing the OA amount would less vary the CO_2 desorption area of α peak, and when OA/Co was 2/2, its α peak area was slightly bigger than other samples.

With an increase of EG/Co, the α peak shifted to lower temperature (Fig. 10C), implying that the presence of ethylene glycol facilitate the dispersion of iron species in Co_3O_4, leading to easier reaction of the superficial oxygen species with CO adsorbed. And the β peak area increased obviously with increasing EG amount. As shown in Fig. 10D, the effect of the calcination temperature on the CO_2-TPD spectra of the $Fe_3Co_{16}O_x$ catalyst was remarkable. With increasing the calcination temperature, the peak temperature of CO_2 desorption shifted lower, and for the $Fe_3Co_{16}O_x$ calcined at 250 °C it exhibited the lowest peak temperature (~110 °C) and the largest peak area. When the calcination temperature is higher (over 250 °C), the CO_2 desorption peak temperature shifted higher and the peak area decreased.

The results of O_2-TPD (Fig. S5) show that the presence of Fe in the $Fe_3Co_{16}O_x$ catalyst increases remarkably the surface adsorbed monatomic species O^- (ad) and the lattice oxygen O^{2-} (ad/lattice). In the preparation of catalyst, the ethylene glycol amount would affect unobviously the desorption peaks of oxygen species. The catalyst calcined at 250 °C possessed much more amount of O^-(ad) and surface lattice oxygen O^{2-} than the catalyst calcined at >250 °C. These results show that the high adsorption ability for CO and the much more surface oxygen species of the $Fe_3Co_{16}O_x$ catalyst calcined at 250 °C are the reason of its high CO catalytic activity and stability.

3.4.7. *In situ* DRIFTS studies

The catalytic performance testing demonstrated that the presence of H_2O has a great influence on the CO oxidation over the $Fe_3Co_{16}O_x$ catalyst. Here, *in situ* DRIFT spectroscopy was used to investigate the effect of water in the reactant gas on the CO catalytic oxidation. *In situ* DRIFT spectra of CO oxidation on the $Fe_3Co_{16}O_x$ catalyst at 70 °C are shown in Fig. 11.

In the IR spectra in Fig. 11, the band at 3300–3700 cm^{-1} are attributed to the stretching vibration of OH groups [61]; the peaks at 2375 and 2330 cm^{-1} are assigned to the adsorbed CO_2 [23]; the bands at 2170 and 2110 cm^{-1} are due to the CO species adsorbed

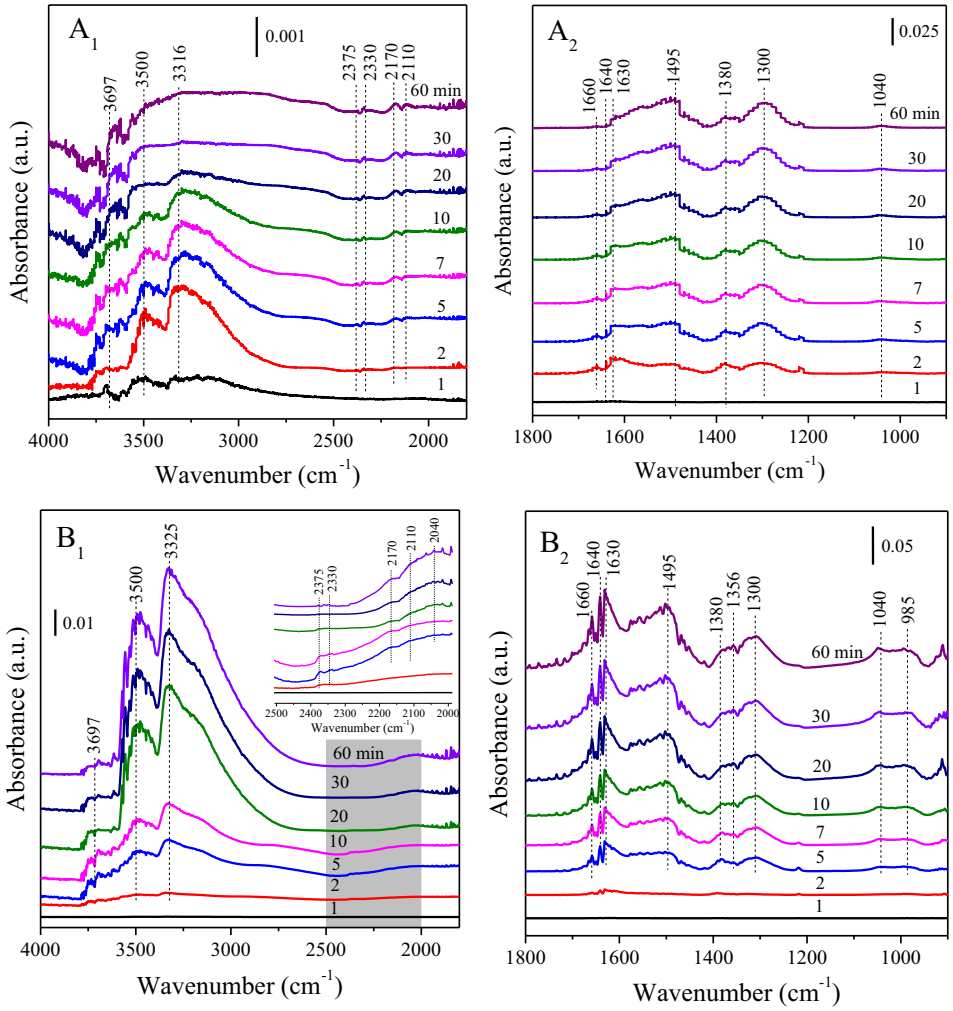

Fig. 11. *In situ* DRIFT spectra of the $Fe_3Co_{16}O_x$ catalyst at 70 °C in the reactant gas (50 mL/min) of 0.15% CO, 18.9% O_2 balanced N_2 and (A) 3–10 ppm H_2O and (B) ~0.6 vol.% H_2O.

on the cobalt sites [35], in which the peak shift is due to back donation of electrons to 2π orbitals of adsorbed CO on the catalyst by adding Fe [23]. The band located at 1660 cm^{-1} is associated with the adsorbed bicarbonate species on the surface [62]; the bands at 1640 and 1630 cm^{-1} are assigned to the deformation vibration of OH groups on carboxyl species [63]; the carbonate peaks at 1495, 1380 and 1300 cm^{-1} demonstrate that CO adsorbed on the $Fe_3Co_{16}O_x$ catalyst have formed the monodentate and bidentate carbonate species [53]; the peak at 1450 cm^{-1} may be attributed to the carbonate adsorbed on the Fe^{3+} sites [24,46]; the band at 1356 cm^{-1} is attributed to the formate species resulted from the reaction of CO and hydroxyl groups adsorbed ($CO^* + OH^* \rightarrow COOH^* + *$) on the cobalt ferrite surface [23]; the peaks at 985 and 1040 cm^{-1} are assigned to perturbed O_2^{x-} (intermediate between O_2^- and O_2^{2-}) [16], and the band at 2040 cm^{-1} might be a strong interaction between CO and Lewis acidic sites on the catalyst surface [24].

With an increase in the reaction time in the normal reaction condition (3–10 ppm H_2O) (Fig. 11(A_1, A_2)), the OH groups (at 3697, 3501, 3310, 1640 and 1630 cm^{-1}) decreased and disappeared after 30 min, which shows that the OH groups have participated in the CO oxidation, and the carbonate species (at 1495, 1380 and 1300 cm^{-1}) on the surface and CO_2 adsorbed (at 2375 and 2330 cm^{-1}) increased. And the adsorption of CO on the catalyst (at 2170 and 2110 cm^{-1}) was increased also, and the strengthening of the peak at 1040 cm^{-1} means that more oxygen bonded to low-coordination cobalt sites. These results suggest that the surface oxygen species reacted with CO to form CO_2 and surface carbonates, thus forming the coordinatively unsaturated cobalt sites and oxygen vacancies on the surface under normal condition (3–10 ppm H_2O).

In the moisture-rich condition (~ 0.6 vol.% H_2O) (Fig. 11(B_1, B_2)), the OH groups did not disappear after 30 min and the intensities of these absorption peaks were more and more with the time, which shows that abundant H_2O covered on the surface of catalyst, resulting in the deactivation of the $Fe_3Co_{16}O_x$ catalyst in CO oxidation. And not only the high vapor concentration hardly weakened the intensities of IR absorption bands of carbonates on the surface, but also enhanced their intensities, indicating that the presence of water promoted the formation of carbonates and formed carbonates may be one of intermediates. In addition, some new bands around 1356, 2040 and 985 cm^{-1} formed.

For CO adsorption, most researchers thought that CO adsorbed on the Co^{3+} sites [1,16,54,64] or Co^{2+} sites [35], and some suggested that CO adsorbed on both Co^{3+} and Co^{2+} sites [25,53,65]. Pollard et al. reported that CO adsorbed on Co^{2+} and found a IR absorption band of CO-Co^{2+} at 2006 cm^{-1} [35]. In this work, the IR absorption band at around 2006 cm^{-1} cannot be found, hence, it seems more possible that CO adsorbed on Co^{3+} and not Co^{2+} sites. For the CO catalytic oxidation over $Fe_3Co_{16}O_x$ catalyst, we consider that it

follows the Mars-van Krevelen mechanism, CO adsorbed on Co^{3+} extracts adjacent lattice oxygen to form Co^{2+}, CO_2 and oxygen vacancies [20,33], and then O_2 adsorbs in the oxygen vacancy and oxidizes Co^{2+} to Co^{3+}. The results of DRIFTS under moisture rich condition showed that the presence of water promoted the formation of more carbonate species by adsorbed CO reacting with surface OH-* ($CO^* + OH^* \rightarrow COOH^* + *$, * is the adsorption site), and the formation of carbonate species on the surface might cover the active sites, thus leading to the deactivation of catalyst [25]. The polymer nano-film coated on the surface of $Fe_3Co_{16}O_x$ catalyst can isolate water molecules from the coated metal oxides to inhibit water molecules adsorbing on the active sites of catalyst, and further restraining the formation of carbonates on the metal oxide catalyst and improving the water-resistance of the oxides catalysts.

4. Conclusions

In summary, the polymer nanofilm coated Co-Fe mixed oxide ($Fe_aCo_bO_x$) catalyst was synthesized by a solid-phase method mediated with oxalic acid (OA)/ethlyene glycol (EG). The effects of Fe doping amount, OA and EG amounts and calcination temperature on the physicochemical and catalytic properties of the $Fe_aCo_bO_x$ catalysts were investigated. The nanofilm-coated $Fe_3Co_{16}O_x$ nanoparticles calcined at 250 °C possesses the highest surface area (134 m^2/g), the highest Co^{3+}/Co^{2+} ratio (1.89) and the highest oxygen vacancy (20.5%), and thus exhibits the best catalytic performance, such as, T_{50} of −114 °C under normal moisture (3–10 ppm water) and T_{50} of 47 °C under moisture-rich (~0.6 vol. %). Remarkably, for the low-cost transition metal oxide catalysts, the excellent and unprecedented long-term catalytic stability (> one month) with almost zero activity loss has been achieved even at a high moisture level (3.1 vol.%) and relatively low temperature (90 °C), in which polymer nanofilm coating and iron-incorporation induced chemical/structural changes played major roles in CO oxidation, particularly under moisture condition. In addition, the following conclusions can be obtained.

(1) The simultaneous formation of the polymer nanofilm and Co-Fe oxide nanocrystals are particularly important for both high activity and long term stability, in which the polymer nanofilm restricts the growth of the catalyst nanocrystals, and at the same time seals the catalyst seamlessly.
(2) Adding an appropriate amount of Fe to Co_3O_4 can facilitate the generation of more structural defects and higher Co^{3+}/Co^{2+} ratio, as well as higher oxygen vacancy and reactive surface oxygen levels, resulting in the high performance of the $Fe_3Co_{16}O_x$ catalyst.
(3) Appropriate polymer precursors, catalyst components and synthesis conditions are all critical in the preparation of the polymer nanofilm coated catalyst, and further optimizations are underway in improving the catalyst performance under moisture condition.

Our long term goal with this newly conceptualized polymer nanofilm coated catalysts is to be able to detoxicate various harmful gases (not limited to carbon monoxide) under various ambient conditions.

Acknowledgments

This study was financially supported by the National Natural Science Foundation of China (21273150, 21571061), the National Basic Research Program of China (2013CB933201), the National High Technology Research and Development Program of China (2015AA034603, 2012AA062703).

Appendix A. Supplementary material

Supplementary data associated with this article can be found, in the online version, at http://dx.doi.org/10.1016/j.jcat.2017.06.022.

References

[1] S. Royer, D. Duprez, ChemCatChem 3 (2011) 24.
[2] Y. Yu, T. Takei, H. Ohashi, H. He, X. Zhang, M. Haruta, J. Catal. 267 (2009) 121.
[3] C.H. Kuo, W. Li, W. Song, Z. Luo, A.S. Poyraz, Y. Guo, A.W. Ma, S.L. Suib, J. He, A.C. S. Appl, Mater. Interfaces 6 (2014) 11311.
[4] L. Liu, F. Zhou, L. Wang, X. Qi, F. Shi, Y. Deng, J. Catal. 274 (2010) 1.
[5] G. Chen, Y. Zhao, G. Fu, P.N. Duchesne, L. Gu, Y. Zheng, X. Weng, M. Chen, P. Zhang, C.W. Pao, J.F. Lee, N. Zheng, Science 344 (2014) 495.
[6] D.A.H. Cunningham, T. Kobayashi, N. Kamijo, M. Haruta, Catal. Lett. 25 (1994) 257.
[7] L. Nguyen, S. Zhang, S.J. Yoon, F. Tao, ChemCatChem 7 (2015) 2346.
[8] K. An, S. Alayoglu, N. Musselwhite, S. Plamthottam, G. Melaet, A.E. Lindeman, G.A. Somorjai, J. Am. Chem. Soc. 135 (2013) 16689.
[9] S. Bonanni, K. Aït-Mansour, W. Harbich, H. Brune, J. Am. Chem. Soc. 136 (2014) 8702.
[10] Z. Hu, X. Liu, D. Meng, Y. Guo, Y. Guo, G. Lu, ACS Catal. 6 (2016) 2265.
[11] G. Li, L. Li, Y. Yuan, J. Shi, Y. Yuan, Y. Li, W. Zhao, J. Shi, Appl. Catal. B 158–159 (2014) 341.
[12] Y. Shen, Y. Guo, L. Wang, Y. Wang, Y. Guo, X. Gong, G. Lu, Catal Sci. Technol. 1 (2011) 1202.
[13] Y. Liu, H. Dai, J. Deng, S. Xie, H. Yang, W. Tan, W. Han, Y. Jiang, G. Guo, J. Catal. 309 (2014) 408.
[14] M.S. Chen, D.W. Goodman, Science 306 (2004) 252.
[15] X. Xie, Y. Li, Z.Q. Liu, M. Haruta, W. Shen, Nature 458 (2009) 746.
[16] J. Jansson, A.E.C. Palmqvist, E. Fridell, M. Skoglundh, L. Österlund, P. Thormählen, V. Langer, J. Catal. 211 (2002) 387.
[17] S. Yao, K. Mudiyanselage, W. Xu, A.C. Johnston-Peck, J.C. Hanson, T. Wu, D. Stacchiola, J.A. Rodriguez, H. Zhao, K.A. Beyer, K.W. Chapman, P.J. Chupas, A. Martínez-Arias, R. Si, T.B. Bolin, W. Liu, S.D. Senanayake, ACS Catal. 4 (2014) 1650.
[18] O.H. Laguna, W.Y. Hernández, G. Arzamendi, L.M. Gandía, M.A. Centeno, J.A. Odriozola, Fuel 118 (2014) 176.
[19] W. Song, A.S. Poyraz, Y. Meng, Z. Ren, S.Y. Chen, S.L. Suib, Chem. Mater. 26 (2014) 4629.
[20] J. Li, G. Lu, G. Wu, D. Mao, Y. Guo, Y. Wang, Y. Guo, RSC Adv. 3 (2013) 12409.
[21] M. Zhou, L. Cai, M. Bajdich, M. García-Melchor, H. Li, J. He, J. Wilcox, W. Wu, A. Vojvodic, X. Zheng, ACS Catal. 5 (2015) 4485.
[22] D. Gu, C.J. Jia, C. Weidenthaler, H.J. Bongard, B. Spliethoff, W. Schmidt, F. Schüth, J. Am. Chem. Soc. 137 (2015) 11407.
[23] C.A. Chagas, E.F. de Souza, M.C.N.A. de Carvalho, R.L. Martins, M. Schmal, Appl. Catal., A 519 (2016) 139.
[24] F. Grillo, M.M. Natile, A. Glisenti, Appl. Catal., B 48 (2004) 267.
[25] H.F. Wang, R. Kavanagh, Y.L. Guo, Y. Guo, G.Z. Lu, P. Hu, Angew. Chem., Int. Ed. 51 (2012) 6657.
[26] X. Xu, X. Sun, H. Han, H. Peng, W. Liu, X. Peng, X. Wang, X. Yang, Appl. Surf. Sci. 355 (2015) 1254.
[27] C.H. Chen, E.C. Njagi, S.P. Sun, H. Genuino, B. Hu, S.L. Suib, Chem. Mater. 22 (2010) 3313.
[28] T. Biemelt, K. Wegner, J. Teichert, M.R. Lohe, J. Martin, J. Grothe, S. Kaskel, Appl. Catal. B 184 (2016) 208.
[29] T. Biemelt, K. Wegner, J. Teichert, S. Kaskel, Chem. Commun. 51 (2015) 5872.
[30] X.D. Hou, Y.Z. Wang, Y.X. Zhao, Catal. Lett. 123 (2008) 321.
[31] M. Lv, X. Guo, Z. Wang, L. Wang, Q. Li, Z. Zhang, RSC Adv. 6 (2016) 27052.
[32] Y. Lou, L. Wang, Z. Zhao, Y. Zhang, Z. Zhang, G. Lu, Y. Guo, Y. Guo, Appl. Catal. B 146 (2014) 43.
[33] Y. Lou, J. Ma, X. Cao, L. Wang, Q. Dai, Z. Zhao, Y. Cai, W. Zhan, Y. Guo, P. Hu, G. Lu, Y. Guo, ACS Catal. 4 (2014) 4143.
[34] Y. Lou, X.M. Cao, J. Lan, L. Wang, Q. Dai, Y. Guo, J. Ma, Z. Zhao, Y. Guo, P. Hu, G. Lu, Chem. Commun. 50 (2014) 6835.
[35] M.J. Pollard, B.A. Weinstock, T.E. Bitterwolf, P.R. Griffiths, A.P. Newbery, J.B. Paine III, J. Catal. 254 (2008) 218.
[36] X.L. Xu, J.Q. Li, Surf. Sci. 605 (2011) 1962.
[37] L. Li, A. Wang, B. Qiao, J. Lin, Y. Huang, X. Wang, T. Zhang, J. Catal. 299 (2013) 90.
[38] X.Q. Gong, P. Hu, R. Raval, J. Chem. Phys. 119 (2003) 6324.
[39] A. Biabani-Ravandi, M. Rezaei, Z. Fattah, Chem. Eng. Sci. 94 (2013) 237.
[40] L.Q. Qwabe, H.B. Friedrich, S. Singh, J. Mol. Catal. A 404–405 (2015) 167.
[41] F. Zhou, X. Du, J. Yu, D. Mao, G. Lu, RSC Adv. 6 (2016) 66553.
[42] X. Du, H.Y. Li, J. Yu, X. Xiao, Z. Shi, D. Mao, G. Lu, Catal, Sci. Technol. 5 (2015) 3970.
[43] G.R. Bamwenda, S. Tsubota, T. Nakamura, M. Haruta, Catal. Lett. 44 (1997) 83.
[44] Q. Yang, H. Choi, S.R. Al-Abed, D.D. Dionysiou, Appl. Catal. B 88 (2009) 462.
[45] T. Yamashita, P. Hayes, Appl. Surf. Sci. 254 (2008) 2441.
[46] L. Wang, X. Cheng, Z. Wang, C. Ma, Y. Qin, Appl. Catal. B 201 (2017) 636.
[47] S.Y. Chen, W. Song, H.J. Lin, S. Wang, S. Biswas, M. Mollahosseini, C.H. Kuo, P.X. Gao, S.L. Suib, A.C.S. Appl, Mater. Interfaces 8 (2016) 7834.
[48] J.Y. Luo, M. Meng, X. Li, X.G. Li, Y.Q. Zha, T.D. Hu, Y.N. Xie, J. Zhang, J. Catal. 254 (2008) 310.

[49] A.S. Poyraz, C.H. Kuo, S. Biswas, C.K. King'ondu, S.L. Suib, Nature 4 (2013) 2952.
[50] Q. Liu, L.C. Wang, M. Chen, Y. Cao, H.Y. He, K.N. Fan, J. Catal. 263 (2009) 104.
[51] K. Ding, D. Wang, P. Yang, P. Hou, X. Cheng, RSC Adv. 6 (2016) 16208.
[52] Y. Zhao, X. Zhou, Y. Ding, J. Huang, M. Zheng, W. Ye, J. Catal. 338 (2016) 30.
[53] S.A. Singh, G. Madras, Appl. Catal., A 504 (2015) 463.
[54] J. Jansson, J. Catal. 194 (2000) 55.
[55] M.M. Natile, A. Glisenti, Chem. Mater. 15 (2003) 2502.
[56] D. Meng, W. Zhan, Y. Guo, Y. Guo, L. Wang, G. Lu, ACS Catal. 5 (2015) 5973.
[57] Z. Ren, V. Botu, S. Wang, Y. Meng, W. Song, Y. Guo, R. Ramprasad, S.L. Suib, P.X. Gao, Angew. Chem., Int. Ed. 53 (2014) 7223.
[58] X. Mou, Y. Li, B. Zhang, L. Yao, X. Wei, D.S. Su, W. Shen, Eur. J. Inorg. Chem. 2012 (2012) 2684.
[59] M. Kang, M.W. Song, C.H. Lee, Appl. Catal., A 251 (2003) 143.
[60] L. Xue, C. Zhang, H. He, Y. Teraoka, Appl. Catal., B 75 (2007) 167.
[61] B. Debnath, A. Bansal, H.G. Salunke, A. Sadhu, S. Bhattacharyya, J. Phys. Chem., C 120 (2016) 5523.
[62] S. Gaur, H. Wu, G.G. Stanley, K. More, C.S.S.R. Kumar, J.J. Spivey, Catal. Today 208 (2013) 72.
[63] J. Lin, B. Qiao, L. Li, H. Guan, C. Ruan, A. Wang, W. Zhang, X. Wang, T. Zhang, J. Catal. 319 (2014) 142.
[64] X.L. Xu, E. Yang, J.Q. Li, Y. Li, W.K. Chen, ChemCatChem 1 (2009) 384.
[65] H.F. Wang, R. Kavanagh, Y.L. Guo, Y. Guo, G. Lu, P. Hu, J. Catal. 296 (2012) 110.